Ion acceleration in Ar–Xe and Ar–He plasmas. I. Electron energy distribution functions and ion composition

Ioana A. Biloiu[a] and Earl E. Scime
Department of Physics, West Virginia University, Morganton, West Virginia 26506, USA

(Received 3 August 2010; accepted 6 October 2010; published online 9 November 2010)

Electron energy distribution functions (eedf), ion production, and ion composition are studied in Ar–Xe and Ar–He expanding helicon plasmas. It was found that under the conditions of constant total flow rate, Xe, in addition to Ar, changes the eedf from Maxwellian-like to Druyvesteyn-like with a shortening of the high energy tail at ~15 eV. The electron temperature exponentially decreases from ~7 eV in pure Ar plasma to ~4 eV in pure Xe plasma. Xenon ions dominate the ion population for Xe filling fractions greater than 10%. The plasma density increases by ~15% with increasing Xe fraction. For an Ar–He plasma, increasing the helium fraction increases the electron temperature from ~7 eV in pure Ar plasma to ~14 eV for a He filling fraction of 80%. The plasma density drops by more than three orders of magnitude from 1.14×10^{11} cm^{-3} to 6.5×10^{7} cm^{-3}. However, the inferred ion densities indicate that even at a helium fraction of 80%, argon ions significantly outnumber helium ions. © *2010 American Institute of Physics*.
[doi:10.1063/1.3505822]

I. INTRODUCTION

The energetic ion beam generated by the current-free electric double layer (EDL), which spontaneously forms in the magnetic expansion region of low pressure helicon plasma sources,[1] might be an ideal candidate for extraterrestrial spacecraft propulsion.[2,3] Experiments have demonstrated that formation of a current-free EDL in the divergent magnetic field at the end of helicon plasma source[4,5] and the subsequent ion acceleration to supersonic speeds occurs in a wide variety of working gases. Beside argon,[6] ion acceleration in xenon[7] helicon plasma has been demonstrated. Ion beam velocities as high as 11 km/s for Ar^+ and 6 km/s for Xe^+ were measured with a retarding field energy analyzer in the Chi-Kung device. In recent molecular gas experiments in Chi-Kung, ion exhaust speeds of 17 km/s for N_2, 25 km/s for NH_3, and 27 km/s for CH_4 were reported.[8] EDL formation in uniform magnetic fields[9] and in electronegative gas plasma has also been observed.[10–12] To reduce the mass and power requirements, practical helicon sources plasma thrusters are likely to employ permanent magnets.[13–15] The classic signature of an EDL, two distinct ion populations with one highly supersonic, has been observed downstream of a small diameter, compact helicon plasma source employing permanents magnets.[16] Based on ion beam analysis in noble gas plasmas, it has been found that:[17] (a) the minimum gas pressure at which a stable discharge can be sustained and the most efficient ion acceleration occurs is lower in heavier gases (which for noble gases corresponds to lower ionization potentials); and (b) for identical discharge conditions, the ion beam velocity decreases with atomic mass and ranges from 58 km/s in He to 24 km/s in Ar to 13 km/s in Xe. This second observation implies a dependence of ion acceleration on the characteristic Bohm speed (proportional to the inverse of the square root of the ion mass). However, it is difficult to conclusively demonstrate the role of the Bohm speed in defining the final ion speed in different single ion species plasma experiments because of the impossibility of matching the operating conditions (gas pressure, flow rate, input power, etc.) and electron temperature for different working gases. An alternative approach is to investigate ion acceleration in mixed gas plasmas with a single electron temperature. Under such conditions, the ion acceleration controlled by the Bohm velocity will be easier to confirm.

To identify the mechanisms through which ion acceleration takes place in mixed gas helicon plasmas, extensive plasma diagnostics such as planar and cylindrical Langmuir probes (LP), optical emission spectroscopy (OES), and laser induced fluorescence (LIF) coupled with theoretical models have been employed to study ion production, relative plasma ion composition, and ion velocity distribution functions.

Argon is the workhorse in plasma modeling and plasma simulation; consequently, argon plasma characteristics are well documented. Therefore, in this work, mixtures of Ar–Xe and Ar–He with argon ions serving as probes were examined to gain insight into heavier and lighter gas doping effects on ion acceleration mechanisms in expanding helicon plasma. Here we describe Langmuir probe and optical emission spectroscopy analyses of the Ar–Xe and Ar–He plasmas.

II. THE PLASMA SOURCE–EXPANSION CHAMBER SYSTEM

The helicon plasma source used for these investigations consists of two distinct parts [see Fig. 1(a)]: the Hot hELIcon eXperiment (HELIX) source where high density plasma is created, and an expansion chamber, Large Experiment on Instabilities and Anisotropies (LEIA) into which the plasma flows. HELIX consists of a 61 cm long, 10 cm diameter Pyrex tube coaxially mated with a 91 cm long, 15 cm diameter stainless steel tube. LEIA is a 4 m long, 2 m diameter

[a]Author to whom correspondence should be addressed. Electronic mail: iabiloiu@yahoo.com.

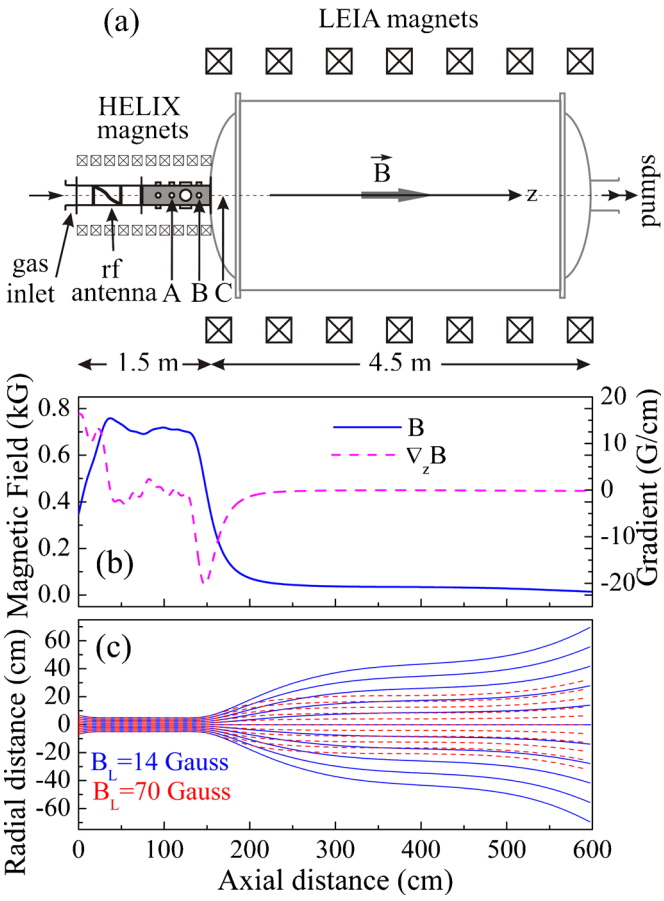

FIG. 1. (Color online) (a) The helicon source (HELIX)-diffusion chamber (LEIA) system. LP measurement were performed at locations A (z=126 cm) and C (z=169 cm); LIF measurements were performed at locations B (z=146 cm) and C (z=169 cm). (b) Magnetic field profile and magnitude, and magnetic field gradient vs axial position over the entire length of HELIX-LEIA system. (c) Contours of constant magnetic flux showing the increased divergence that results when the magnetic field in the expansion region decreases from 70 G (dashed line) to 14 G (solid line) for a constant source field of 600 G.

aluminum diffusion chamber. Ten water cooled solenoids create the axial magnetic field in HELIX. Two dc power supplies (Xantrex XFR) connected in parallel provide up to 400 A current for the electromagnets. The maximum attainable magnetic field is 1200 G. Seven 9 in. diameter water cooled electromagnets confine the plasma in the downstream chamber. A current of up to 200 A is provided by an electromagnetic interference dc power supply and the maximum achievable axial magnetic field in LEIA is 140 G. Figure 1(b) shows the on-axis magnetic field strength and its gradient in the HELIX-LEIA combined system as calculated with a two-dimensional numerical model that was validated with measurements along the system axis. The evolution of contour lines of constant magnetic flux (flux tubes) is shown in Fig. 1(c) for a constant magnetic field strength in HELIX of 600 G and for two magnetic field strengths in LEIA: 70 G (dash line) and 14 G (solid line). Under typical operating conditions, in the connection region between the helicon source and the expansion chamber, there is an axial magnetic field gradient of nearly 10 G/cm over a distance of 70 cm.

The HELIX-LEIA system is pumped by two 1600 l turbomolecular pumps with membrane backing pumps, both located at the end of LEIA opposite of HELIX. The gas inlet valve is in HELIX near the rf antenna. HELIX-LEIA is a freely expanding plasma system having a physical expansion ratio (the diffusion chamber cross-sectional area divided by the plasma source tube cross-sectional area) of ~1.8. Since the gas inlet port is at the end of HELIX opposite LEIA and the vacuum pumping port at the end of LEIA, there is a pressure gradient along the source axis; in the expansion chamber the pressure is nearly constant and almost one order of magnitude smaller than the pressure in HELIX. The gas (or gas mixture) flow rate is controlled by two calibrated mass flow valves (MKS 1179) with a flow controller (PR-4000). The flow controller regulates the flow of argon up to 200 SCCM with an accuracy of 1%, and the flow of helium or xenon up to 20 SCCM with an accuracy of 0.1%.

The rf power used for plasma generation in HELIX is supplied by a 30 dB rf amplifier (ENI 1000) in conjunction with a 50 MHz function generator (Wavetek model-80). The rf power is transmitted from the amplifier to the source through a high frequency coaxial cable and a π-type matching network to match the 50 Ω output impedance of the amplifier to the variable plasma impedance. A 19 cm long, half wave, m=+1, helical antenna couples the rf energy into the plasma. The antenna is tightly wrapped around the Pyrex tube at 37 cm from the closed end of HELIX.

III. PLASMA DIAGNOSTICS

A. Langmuir probe

In a magnetized plasma, the Langmuir probe I-V characteristic is affected by the local magnetic field.[18] Magnetic fields are strong enough to make the electron Larmor radius smaller than the probe radius limit electron saturation current to only a few tenths of ion saturation current. The characteristic "knee"[19] in this case is indistinct and the I-V curve is exponential only over a range of a few k_BT_e above the floating potential. For the weak magnetic fields in LEIA (~10 G), the electrons are unmagnetized (electron cyclotron radius $r_{ce}\cong 5$ mm larger than probe radius r_p=0.5 mm) and the magnetic field effects can be ignored. For HELIX, magnetic fields ~700 G, the electron cyclotron radius ($r_{ce}\sim 70$ μm) is sevenfold smaller than the probe radius and magnetic effects must be included in the analysis. According to Laframboise and Rubinstein,[20] even in strong magnetic fields the electron phase-space density or velocity distribution function can still be described by the usual Maxwell–Boltzmann distribution with an additional correction term for a hypothetical potential well arising from the presence of the magnetic field. Since the electron distribution is not distorted but only shifted in energy, measurements obtained by applying the unmagnetized probe theory to the eedf data corrected for energy shift still provide an accurate measure of density, potential, and electron temperature in magnetized plasmas.

For a simple, unmagnetized, collisionless, Maxwellian plasma comprised of one electron population and two posi-

tive ions species, the collected current for applied voltages around the floating potential is given by the sum of electron and ion Bohm currents[21,22]

$$I(V) \cong eA_p\left(n_{i1}\sqrt{\frac{k_BT_e}{M_1}} + n_{i2}\sqrt{\frac{k_BT_e}{M_2}}\right) \times\left(\frac{n_e}{n_{i1}\sqrt{2\pi m_e/M_1} + n_{i2}\sqrt{2\pi m_e/M_2}}e^{eV/k_BT_e} - \frac{A_S}{A_p}e^{-1/2}\right), \quad (1)$$

where m_e and $M_j, j=1,2$, are the electron and ion masses, respectively; n_e and n_{ij} are electron and ions densities; A_p is the probe area; and A_S is the sheath area. At high plasma densities ($>10^{11}$ cm^{-3}), the sheath around a negatively biased probe is so thin that the surface area of the sheath is essentially the same as the surface area of the probe, $A_S=A_p$. Equivalently, the ratio of the probe radius to the Debye length is larger than 1. In contrast to a single ion species plasma for which the plasma potential, electron temperature, and plasma density can be directly determined from the *I-V* trace[23] for a two ion species plasma, the plasma density and plasma potential cannot be uniquely determined. In such a case, determination of the electron density, the effective electron temperature T_{eff} (which corresponds to a mean electron energy $\langle\varepsilon\rangle$), and the plasma potential V_p from the eedf is accomplished through the Druyvesteyn procedure.[24] The Druyvesteyn technique consists of differentiating the probe characteristic to obtain the eedf and then determining n_e and T_{eff} from integrals of the eedf. The advantage of Druyvesteyn's method is that it can be used for non-Maxwellian plasmas in which the electron density is not simply related to a single electron temperature and the ion saturation current. Perhaps even more important for the measurements presented in this work is that the classical Langmuir technique is not generally applicable for multi-ion species plasmas; especially when only the ion portion of the *I-V* characteristic is used. Because the velocity of the ions entering the sheath (the Bohm velocity) significantly differs from the single ion species case, the use of the Langmuir analysis could lead to greatly exaggerated values for the electron density.

For a cylindrical Langmuir probe, the eedf is obtained from the second derivative of the collected current with respect to the applied probe voltage V

$$f(\varepsilon) = \frac{2(2m)^{1/2}}{e^3A_p}\varepsilon^{1/2}\frac{d^2I_e}{dV^2}. \quad (2)$$

The maximum of the first derivative or the zero crossing of the second derivative of the probe current with respect to the applied voltage is used to determine the plasma potential. In practice, it is easier to work with another function called electron energy probability function (eepf),[25] $F(\varepsilon) = \varepsilon^{-1/2}f(\varepsilon)$ because it distinguishes between different energy distribution functions. For example, on a logarithmic plot a Maxwellian eepf is a straight line[26] and a Druyvesteyn distribution (used to characterize an eedf that is depleted at high energies) is a parabola.

Once the electron distribution function is known, the electron density is obtained by integrating the eedf over all possible energies

$$n_e = \int_0^\infty f(\varepsilon)d\varepsilon, \quad (3)$$

and the effective electron temperature is obtained from the weighted average of the electron energy $\langle\varepsilon\rangle$

$$T_{\text{eff}} = \frac{2}{3}\langle\varepsilon\rangle = \frac{2}{3n_e}\int_0^\infty \varepsilon f(\varepsilon)d\varepsilon. \quad (4)$$

For a planar probe aligned perpendicular to the plasma flow (the z axis in the HELIX-LEIA system), the electron flux entering the sheath only depends on the z velocity component, v_z. Therefore for this one-dimensional geometry the eedf is obtained from the first derivative of the *I-V* characteristic[27,28]

$$f(v_z) = \frac{m}{e^2A_p}\frac{dI_e}{dV}. \quad (5)$$

As for the cylindrical probe case, the electron density is directly determined from the normalization condition and the effective electron temperature from the mean electron energy $\langle\varepsilon_z\rangle$ along one degree of freedom.[29]

In this work, both cylindrical and planar (disk) Langmuir probes were used. The cylindrical probe consists of a 0.5 mm diameter graphite rod that extends 3 mm from an insulating alumina tube. The planar probe is fabricated from a tungsten sheet cut into a circle and spot welded to a tungsten rod. The diameter of the disk is 6 mm. One side of the probe surface is coated with alumina powder to prevent current collection. The tungsten rod, which is 2.5 cm long, is shielded from the plasma with an alumina tube.[30] Both probes are rf compensated. The compensation is accomplished by a series of rf chokes covering the frequency range of 6–18 MHz and a 10 nF shorting capacitor. Although slightly more difficult to construct, the planar probe has the important advantage of being able to reach electron saturation in a high density, magnetized, helicon plasma.

The full eedfs were recovered from the retarded electron component of the probe data. The challenge in using Eqs. (2) and (5) to obtain electron energy distribution functions arises from the numerical differentiations of imperfect data. In this work, the probe data were digitally recorded and postprocessed with finite difference and curve fitting algorithms to smooth and differentiate the signals. Oversampling and averaging over many realizations also helped to reduce noise levels in the measurements. Overly aggressive smoothing of the data was avoided so as to not wash out real features in the eedfs. The differentiation process always affects energy resolution at lower energies, leading to a small gap between the eepf peak and the 0 energy value (zero crossing). However, as long as the gap width does not exceed the electron temperature, the eepf measurement is still accurate because the zero crossing is relatively unaffected for a few eV residual gap.[26]

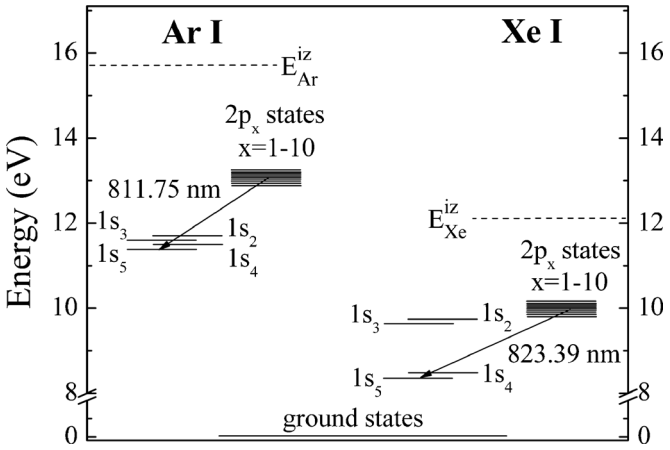

FIG. 2. Partial energy level diagrams for argon and xenon neutrals and the transitions used for OES investigations; the ionization levels are shown by horizontal dashed lines; $1s_3$ and $1s_5$ are metastable states; $1s_2$, $1s_4$, and $2p_x$ are radiative states (adapted from Refs. 31 and 42).

B. Optical emission spectroscopy

The combined Langmuir probe and optical emission spectroscopy measurements were used to quantitatively determine the neutral and ion densities in a helicon plasma that contains a mixture of argon and xenon. In low pressure, weakly ionized plasmas, the number of atoms (or ions) in an excited state can be calculated with a Corona model. Under corona equilibrium conditions, the electron excitation rate and radiative decay rates are equal. Therefore, quantitative information on different specie concentrations can be obtained from the intensities of the emission lines. A Corona model is appropriate for LEIA plasmas, but for the relatively high plasma densities attained in HELIX ($\geq 10^{11}$ cm^{-3}), secondary processes such as excitation from metastable levels cannot be neglected. Therefore, to accurately model the emission line intensities, the Corona model has to be extended to include excitation and/or ionization from metastable levels as well as the ground state.

An energy level diagram for both argon and xenon neutrals is shown in Fig. 2. Argon and xenon atoms may be excited by electron collisions from their ground states to the Paschen 2p levels. These excited levels decay on a short time scale (~20 ns) to one of four levels (in Paschen notation, the short lived $1s_2$ and $1s_4$, and the metastable $1s_3$ and $1s_5$ states) and emit photons in the near-infrared region. Alternatively, electron impact excitation can occur from the ground states to levels above the 2p manifold. These levels also decay on a short time scale, accompanied by emission of a vacuum ultraviolet photon when decaying to the ground state, or longer wavelength photons when decaying to the 2p or higher-lying levels. Decays to levels above the 2p levels are followed by a cascade that increases the intensity of emission from the 2p levels. Thus, when trying to model the intensity of spectral lines originating from the 2p levels, the cascade pathways must be included. Fortunately, cascade effects are automatically included if measured optical cross-sections are used in the rate coefficients calculations instead of the theoretical cross-section values. In addition to excitation from the ground state, electron impact excitation from the metastable levels $1s_3$ and $1s_5$ can populate the argon and xenon Paschen 2p levels for higher plasma densities. The peak cross-section values for direct excitation from the metastable levels to the 2p levels are much larger (15–700 times larger) than those for excitation from the ground state.[31] Therefore, this mechanism must also be included in the particle balance equations. The other two low-lying 1s Paschen states, $1s_2$ and $1s_4$, have short radiative lifetimes and decay to the ground state. Therefore, their population is much lower than the $1s_3$ and $1s_5$ metastable states and consequently their contribution to the 2p population levels through electron impact excitation is negligible.[32]

If the only excitation paths to an upper level j are electron impact excitation from the ground and metastable states and the deexcitation path is radiative decay, the rate equation for the upper level j is

$$dn_j/dt = n_e n_0 k_{0\to j} + n_e n_m k_{m\to j} - n_j/\tau_j, \tag{6}$$

where n_e, n_0, n_m, and n_j are the electron, neutral atom in the ground state, neutral metastable state, and neutral j level densities; τ_j is the radiative lifetime of the jth level; and $k_{0,m\to j}$ are the excitation rate coefficients for electron impact excitation from ground and metastable levels, respectively, to level j. The electron impact rate coefficients are given by the average

$$k_{0,m\to j} = \langle v_e \sigma_{0,m\to j} \rangle = \sqrt{\frac{2}{m_e}} \int_0^\infty f(\varepsilon) \varepsilon^{1/2} \sigma_{0,m\to j}(\varepsilon) d\varepsilon, \tag{7}$$

where v_e, m_e, and ε are the electron velocity, electron mass and energy, respectively, and $\sigma_{0,m\to j}$ is the cross-section for electron excitation from level 0 or m to level j.

Assuming steady state in Eq. (6), the observed emission intensity I_{jk} of a plasma species A at wavelength λ_{jk} corresponding to a quantum transition from upper level j to a lower level k is given by[33]

$$I_{jk} = \frac{hc}{4\pi\lambda_{jk}} S(\lambda_{jk}) b_{jk} n_e n_0 k_{0\to j} \left(1 + \frac{n_m k_{m\to j}}{n_0 k_{0\to j}}\right), \tag{8}$$

where $S(\lambda_{jk})$ is the detection system sensitivity (lenses, optical fibers, spectrometer, and charge-couple device (CCD) camera) at λ_{jk}, $b_{jk}=A_{jk}/\Sigma_{l<j}A_{jl}$ is the branching ratio for the transition $j\to k$, n_0 is the number density in ground state, and n_m is the number density in the metastable state, m. If the intensities of two lines belonging to two different species A and B are used, then the intensity ratio is a function of their population ratio. With an electron energy distribution function obtained from Langmuir probe measurements and the excitation cross-sections available in the literature, the excitation rate coefficients can be calculated. Then from OES measurements of line intensities, the neutral densities of each species in a plasma mixture (Ar and Xe for this study) can be estimated. The situation for the intensity of ionic lines is much more complicated. Excitation to an excited ion state may occur by a one-step process (simultaneous excitation and ionization from the ground state of the neutral atom) or a two-step process (ionization of the neutral atom and then subsequent excitation). However, since for typical low temperature plasma, only few electrons have enough energy for

the one-step process, the largest contribution to an excited ion state population is from excitation of ground state ions. For the particular case of Ar–Xe plasma, the lowest lying ion metastable levels are at relatively low energies (13.48 eV for Ar^+ and 11.26 eV for Xe^+). Thus, the contribution to the excited ionic state population from metastable levels has to be included in the ion population balance equations as well.

For the optical emission spectroscopy investigations reported in this paper, the light emitted by the helicon plasma source is collected and sent through a multimode optical fiber to the entrance slit of the spectrometer. The spectrometer is a 1.33 m Czerny–Turner double pass scanning monochromator (McPherson 209). The dispersive element is a 120 $\times$ 140 mm grating having 1200 lines/mm blazed at 750 nm. The detector is an air cooled dual autofocusing CCD camera (Santa Barbara Instr. Group ST-7) with a 765$\times$510 pixel array at 9 μm/pixel. The quantum efficiency of the camera is between 0.6 and 0.8 for our spectral range of interest. Wavelength calibration was performed with the help of an argon pen lamp and Ar neutral lines tables available from the NIST website.[34] Spectral sensitivity correction factors were obtained from calibration of the relative spectral response of the entire optical path for the spectrometer achievable wavelength range of 400–1000 nm. The calibration was performed by using the tabulated spectral irradiance and the experimentally measured spectrum of a tungsten ribbon lamp (Oriel™).[35]

IV. EEDF AND PLASMA COMPOSITION IN TWO-ELECTROPOSITIVE SPECIES PLASMA

In these experiments, the electron energy distribution function (eedf), ion production, and absolute ion densities were investigated as a function of plasma composition. Ideally, the control of the relative gas composition in mixed gas plasmas is accomplished through direct measurement and control of partial gas pressures. However, the only adjustable gas parameter for these experiments was the mass flow rate of each species. Therefore, different Ar/Xe and Ar/He mixing ratios were obtained by varying Ar, Xe, and He individual mass flow rates.

A. Electron temperature and plasma density in Ar–Xe plasma

To investigate the effects of the gas composition on plasma parameters, electron energy distribution functions were obtained from Langmuir probe measurements taken on the axis of the system, at the middle of HELIX, at z=126 cm ($\sim$70 cm downstream from the antenna; location A in Fig. 1), and in the expansion chamber, at z=169 cm (19 cm downstream of the HELIX-LEIA junction; location C in Fig. 1).

The Ar/Xe ratio was varied by adjusting Ar and Xe individual mass flow rates while holding the total flow rate constant at 10 SCCM (SCCM denotes standard cubic centimeters per minute). The estimated error in gas composition determination due to the slight difference in actual Ar and Xe gas pressures (1.3 mTorr for Ar and 1.5 mTorr for Xe at 10 SCCM in HELIX, respectively, 0.14 and 0.16 mTorr in LEIA) is less than 7%.

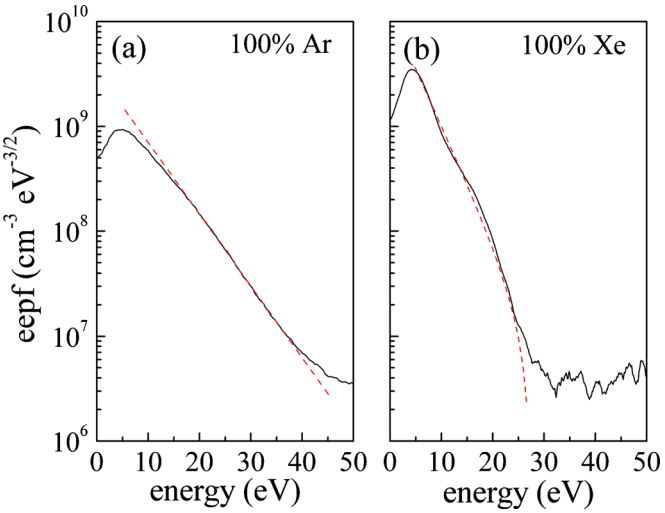

FIG. 3. (Color online) Electron energy probability functions for (a) pure argon plasma and (b) pure xenon plasma.

From the gas ionization point of view, there are large differences between Xe and Ar: xenon has a significantly lower ionization threshold energy (12.13 eV versus 15.76 eV for argon), and a larger peak ionization cross-section (5.2 $\times 10^{-16}$ cm^2 versus 2.8$\times 10^{-16}$ cm^2 for argon). These differences are responsible for the dramatic changes in plasma properties that occur with increasing xenon fraction. As shown in Fig. 3, in the pure argon plasma, the eedf is a single Maxwellian (straight line on the semilogarithmic plot). However, for the pure xenon plasma, the eedf is best fit with a Druyvesteyn-like distribution. Although not a perfect Druyvesteyn distribution [only above 10 eV does the distribution obeys the $\sim(3m_e/M)\times(\varepsilon/e\lambda E)^2$ proportionality law, where M, λ, and E stand for neutral mass, the electron collision mean free path and the ambient electric field, respectively, all other quantities having the usual meaning], the measured eedf shows the characteristic depletion of the high electron energy tail. Consistent with the differences in excitation energies and ionization potentials, the breakpoint in the high energy eedf tail (the energy at which the eedf amplitude equals the noise level) decreases by $\sim$15 eV for pure xenon plasma compared to pure argon. With increasing xenon fraction, the electron density increases and there is an increase in the low electron energy population with a simultaneous reduction in the high energy tail of the distribution. The transition from a single Maxwellian distribution to a Druyvesteyn distribution with increasing of the xenon percentage is not gradual. Once the xenon fraction reaches 10%, the eedf is Druyvesteyn-like.

Figure 4 shows the electron temperature and electron density on the axis of the system calculated from the experimentally obtained eedfs as a function of gas composition in mixed Ar/Xe helicon plasma. The operational parameters were as follows: HELIX magnetic field strength of 700 G, LEIA magnetic field strength of 10 G, input power of 750 W, and a rf driving frequency 9.5 MHz. In HELIX, 70 cm

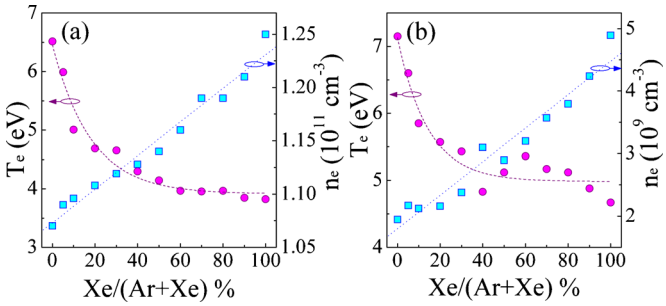

FIG. 4. (Color online) Effective electron temperature and electron density obtained from experimentally obtained eepfs as a function of Ar/Xe composition: (a) at $r=0$ in HELIX, $z=126$ cm; and (b) on the axis of LEIA, $z=169$ cm. The dashed lines are exponential and linear fits for electron temperature and electron density, respectively. Source plasma parameters: $P_{rf}=750$ W, $f=9.5$ MHz, $B_H=700$ G, and $B_L=10$ G.

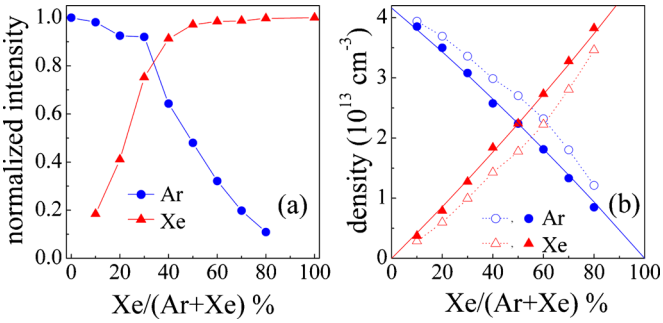

FIG. 5. (Color online) (a) Observed emission line intensities from Ar I (811.75 nm) and Xe I (823.39 nm) lines in HELIX at $z=126$ cm vs xenon fraction; the emission intensities values are normalized to the corresponding pure gases values. The argon emission line intensity was indistinguishable from the background for xenon fractions larger than 80%. (b) Neutral species densities in the plasma as computed from the argon and xenon line intensities ratios: open symbols, Corona model without metastable contribution; full symbols, Corona model with metastable contribution. Solid lines, computed values from the gas flow data.

downstream from the antenna, numerical integrations of the eedfs give an effective electron temperature of 6.5 eV and an electron density of 1.07×10^{11} cm^{-3} for pure Ar plasma; for pure Xe plasma, an effective electron temperature of 3.8 eV and an electron density of 1.25×10^{11} cm^{-3} were obtained. Although the term "electron temperature" has no physical meaning for distributions other than Maxwellian, we use it here for the Druyvesteyn distribution in the sense of average electron energy. Addition of xenon to argon dramatically lowers the effective electron temperature. The decrease in effective electron temperature is exponential with increasing xenon fraction and most of the drop in electron temperature ($\sim$2 eV) occurs as the xenon fraction increases from 0% to 20%. The increase in plasma density with increasing xenon fraction is roughly linear. Under the same operating conditions as previously described but in the expansion chamber, 19 cm downstream of the HELIX-LEIA junction, the effective electron temperature and electron density versus xenon fraction dependencies are shown in Fig. 4(b). The trend in overall effective electron temperature dependence on xenon fraction is similar to what was observed in the source, i.e., an exponential decrease with increasing xenon fraction from $\sim$7.2 eV in pure argon to 4.7 eV in pure xenon. Although almost two orders of magnitude lower, the electron density again linearly increases with increasing of xenon concentration from 2×10^{9} cm^{-3} in pure argon to 5×10^{9} cm^{-3} in pure xenon. The 20-fold to 50-fold higher plasma density in HELIX than in LEIA is explained by the proximity of the antenna and roughly one order of magnitude higher pressure in the source than in the expansion chamber. Better electron thermalization at higher pressure is also responsible for $\sim$1 eV lower electron temperature in the source than in the expansion chamber. The very similar dependencies of the plasma density (linear) and electron temperature (exponential decay with the most of the decrease in the first 20% of Xe addition) versus gas mixing ratio in the source and expansion chamber is consistent with ionization occurring in the source and the plasma convecting into the expansion chamber.

B. Neutral densities from OES observations

Independent of the details of the Corona model used, a major concern when performing any sort of OES analysis is the optical thickness of the plasma at a particular wavelength. As a rule of thumb in choosing the spectral lines for study, transitions to the ground level (resonance lines) or to low lying metastable levels should be avoided because the radiated photons are likely to be reabsorbed by the plasma.[36] For our investigations, we chose the 811.75 nm ($2p_9\rightarrow1s_5$) and 823.39 nm ($2p_6\rightarrow1s_5$) lines for neutral argon and xenon, respectively. Both lines originate from 2p manifolds (see Fig. 2) and terminate on relatively high energy, $1s_5$ metastable levels (11.54 eV for argon and 8.31 eV for xenon above the ground level). Furthermore, given our low operating gas pressure, a small population of the $1s_5$ metastable level is expected, and therefore the plasma might be considered optically thin at these wavelengths.[37]

The emission intensities of the spectral lines of neutral argon and neutral xenon as a function of the xenon fraction, normalized to the measured emission intensities for the corresponding pure gas plasma, collected at $z=126$ cm, are shown in Fig. 5. As expected, the neutral argon emission intensity decreases and the neutral xenon emission intensity increases with increasing xenon fraction. For the general case that includes excitation from metastable states in the model, the ratio of the argon and xenon neutral line intensities given by Eq. (8) is

$$\frac{I_{811}}{I_{823}}=\frac{823}{811}\cdot\frac{S(811)}{S(823)}\cdot\frac{b_{811}}{b_{823}}\cdot\frac{k_{\mathrm{Ar0}}^{811}}{k_{\mathrm{Xe0}}^{823}}\cdot\frac{1+n_{\mathrm{Ar}}^{*}k_{\mathrm{Ar}^{*}}^{811}/n_{\mathrm{Ar}}^{0}k_{\mathrm{Ar0}}^{811}n_{\mathrm{Ar}}^{0}}{1+n_{\mathrm{Xe}}^{*}k_{\mathrm{Xe}^{*}}^{823}/n_{\mathrm{Xe}}^{0}k_{\mathrm{Xe0}}^{823}n_{\mathrm{Xe}}^{0}},\tag{9}$$

where $n_{\mathrm{Ar}}^{0,*}$ and $n_{\mathrm{Xe}}^{0,*}$ are the neutral argon and xenon number densities in the ground "0" and metastable * states, respectively, and $k_{\mathrm{Ar0,}^{*}}^{811}$ and $k_{\mathrm{Xe0,}^{*}}^{823}$ are the argon and xenon electron impact excitation rate coefficients from the ground and metastable states, respectively. The limit of only excitation from

the ground states is obtained from Eq. (9) by setting the metastable densities n^*_{Ar} and n^*_{Xe} equal to zero. In assessing line intensities, the integrated individual line intensities after background removal were considered. The rate coefficients for electron impact excitation of neutral argon and xenon were calculated using Eq. (7) from the experimentally determined eedfs and the optical cross-sections available in the literature.[31,38–40] Since an optically thin plasma was assumed, no corrections for pressure effects on cross-section values resulting from radiation trapping of cascading resonance levels were included.[41]

To calculate the absolute densities of the neutral species, Eq. (9) is combined with the gas kinetic equation

$$p \cong (n^0_{Ar} + n^0_{Xe}) k_B T_{gas}, \tag{10}$$

where p is the total neutral pressure, k_B is the Boltzmann constant, and T_{gas} is the gas temperature (assumed to be uniform throughout the plasma column and equal to the room temperature). The calculated neutral species densities are shown in Fig. 5(b). The branching ratios needed for these computations were calculated based on available transition probabilities and radiative level lifetimes.[42] For the Corona model including metastable contributions to the line intensities, constant ratios of metastable population to the ground state population of 10^{-3} and 3×10^{-3} for argon and xenon, respectively, were assumed.[42]

For the Corona model without metastable contributions, the calculated argon and xenon neutral densities show a slight departure from the expected linear dependence [open symbols in Fig. 5(b)] on gas composition. When metastable contributions are neglected, the calculated argon and xenon neutral densities are equal for a xenon fraction of ~60% =Xe/(Ar+Xe). However, when the metastable excitation terms are included in the model, the dependencies of the OES inferred neutral densities on xenon fraction are linear and the calculated densities are equal for a xenon fraction of ~50% as expected. Given that for the calculation of the excitation rate coefficients the on-axis electron distributions were used but the collected light intensity is line-of-sight integrated, the OES results are in surprisingly good agreement with the neutral densities obtained from the known flow rates, even though this measurement approach ignores any radial profile effects that might occur due to gas depletion.[43] The consistency of the neutral densities determined by OES and the flow rate measurements gives us confidence that the same methodology can provide reliable measurements of the relative ion densities in mixed gas plasma.

C. Partial ion densities in Ar–Xe plasma

In contrast to a single ion species plasma, for two positive ion species plasma the electron density cannot be uniquely determined from a measurement of electron temperature and the ion saturation current. The ion Bohm current contains two unknown ion densities, n_{i1} and n_{i2},

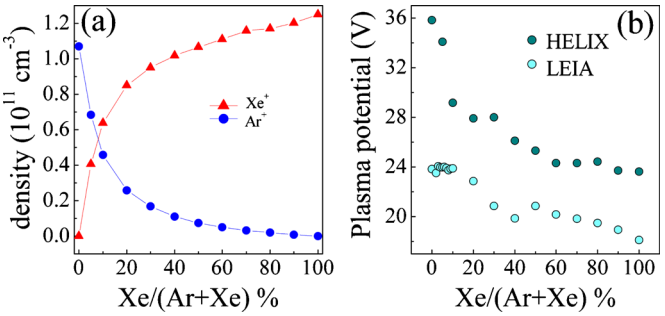

FIG. 6. (Color online) (a) Computed ion densities in HELIX as a function of xenon fraction; and (b) plasma potential in HELIX at $z=126$ cm (dark circles) and in LEIA at $z=169$ cm (light circles) vs xenon fraction.

$$I_{i,sat} = 0.61 e n_e A_p \sum_{j=1}^{2} \frac{n_{ij}}{n_e} \sqrt{\frac{k_B T_e}{M_j}}, \tag{11}$$

which can be related to the electron density through the plasma quasineutrality condition

$$n_{i1} + n_{i2} \cong n_e. \tag{12}$$

For a two-electropositive ion species plasma, Bai *et al.*,[44] assumed that ion densities are related to electron density through the ionization rate constant of each species

$$n_{i1,2}/n_e = p^r_{1,2} k^{iz}_{1,2}/k^{iz}_t, \tag{13}$$

where $p^r_{1,2}$ are the relative partial pressures (relative abundances) of gas species. The ionization rate constants of each species $k^{iz}_{1,2}$ are calculated using the measured electron temperatures, available ionization cross-sections and ionization energies[45]

$$k^{iz}_{1,2} = \sigma^{iz}_{1,2} \left(\frac{8k_B T_e}{\pi m_e}\right)^{1/2} \left(1 + \frac{2k_B T_e}{\varepsilon^{iz}_{1,2}}\right) e^{-\varepsilon^{iz}_{1,2}/k_B T_e}. \tag{14}$$

The total ionization rate constant k^{iz}_t is obtained from the quasineutrality condition as a weighted average of the individual ionization rate constants

$$k^{iz}_t = \sum_{j=1}^{2} p^r_j k^{iz}_j. \tag{15}$$

The absolute total ion density is inferred from either the ion saturation current or the electron density calculated from the integration of the eedf. The calculated Xe^+ and Ar^+ absolute densities versus xenon fraction are shown in Fig. 6(a). Instead of the linear dependence on xenon fraction found for neutral species, an exponential decrease for Ar^+ density and a logarithmic increase for the Xe^+ density are obtained. Roughly equal ion densities of 5.5×10^{10} cm^{-3} are obtained for a xenon fraction of only ~10%. As pointed out earlier, this extreme sensitivity to the xenon fraction results from the 3.7 eV difference in ionization potential between argon and xenon and the twofold larger ionization cross-section for xenon. The combination of these differences causes the electron temperature to rapidly decrease with the xenon fraction [see Figs. 4(a) and 4(b)]. In other words, addition of xenon effectively "clamps" the electron energy distribution function and impedes ionization of argon. Similar dependencies of

Ar^+ and Xe^+ densities versus xenon fraction were observed in capacitively coupled plasmas.[46] In those experiments, the xenon fraction at which equal argon and xenon ion densities were measured was ~15% (Fig. 5 in Ref. 46) in excellent agreement with the value calculated here.

The ion acceleration observed in the proximity of the HELIX-LEIA junction moderately depends on the plasma densities and electron temperatures upstream and downstream of junction (Fig. 4) and strongly on the local plasma potential. Substituting V_p-V_f for V in Eq. (1), the plasma potential is calculated for each gas mixture

$$V_p = V_f - \frac{k_B T_e}{e} \ln\left(\frac{p_1^r k_1^{iz}}{k_t^{iz}} \sqrt{\frac{\pi m}{2M_1}} + \frac{p_2^r k_2^{iz}}{k_t^{iz}} \sqrt{\frac{\pi m}{2M_2}} \right). \quad (16)$$

Figure 6(b) shows the calculated plasma potential in HELIX 70 cm downstream from the antenna and in LEIA 19 cm downstream from the HELIX-LEIA junction. Except for the low Xe concentration (<10%) point, the plasma potentials at those two locations show similar decreasing trends with ~4–5 V higher potentials in the source. For the LEIA measurements, the calculated values based on Eq. (16) are in reasonable agreement with the values directly inferred from either the voltage where the first derivative of the probe *I-V* characteristic attains a maximum or from the point where the second derivative crosses the zero (abscissa). The dependence on Xe concentration for both methods of determining the plasma potential is similar, but there is a consistent difference of ~2–4 V between the inferred values. This difference is likely due to the geometrical correction factor that accounts for the ratio of the probe radius to the Debye length.[47] Because for the data shown in Fig. 6(b) the Debye length varies from 0.45 mm at 100% Ar to 0.23 mm at 100% Xe, inclusion of the correction factor in Eq. (16) would yield plasma potentials ~10–20% smaller; comparable to the difference in plasma potential values calculated with the two methods.

For measurements in HELIX, the plasma potential values inferred from the derivative of the *I-V* characteristic are in fair agreement with those obtained from Eq. (16). Errors in the calculated values arise from the strong magnetic field that shifts the electron distribution in energy[20] and limits the collected electron current[48] as well as from the proximity of the rf antenna to the probe. Since the floating potential was the same, ~1 V, for both pure gas cases, the HELIX data shown in Fig. 6(b) are obtained based on Eq. (16) with V_f=1 V.

D. Partial ion densities in Ar–He plasma

To further investigate the influence of a light mass ion on a heavier ion species, a series of experiments were performed in an Ar–He mixture plasma. The discharge was ignited in pure argon plasma at a total mass flow rate of 10 SCCM. Helium and argon flow rates were then adjusted in a controlled manner so that the total mass flow rate was kept constant and the helium fraction was increased up to 80%. The same source parameters as for the Ar–Xe plasma experiments were used: rf power of 750 W, the rf driving frequency of 9.5 MHz, HELIX magnetic field strength of 700 G, and

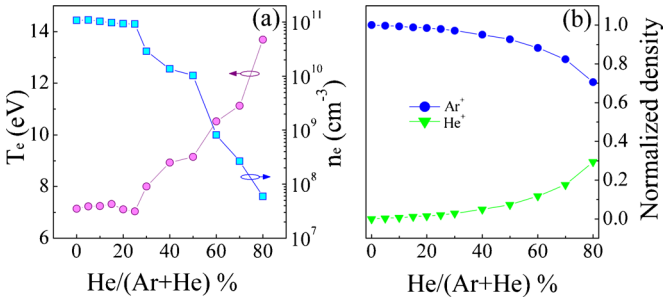

FIG. 7. (Color online) (a) Electron temperature (circles) and electron density (squares) inferred from Langmuir probe measurements in HELIX plasmas at z=126 cm as function of helium fraction; and (b) normalized partial ion densities vs helium fraction in HELIX. Operating conditions: P_{rf}=750 W, f=9.5 MHz, B_H=700 G, and B_L=10 G.

LEIA magnetic field strength of 10 G. By increasing helium fraction, the pressure in HELIX significantly drops from 1.3 mTorr in pure argon down to 0.2 mTorr for a helium fraction of 80%. Further increase of the helium fraction was not possible since the discharge could not be maintained at 750 W of input rf power and such low pressure. With increasing helium fraction, LP measurements taken 70 cm downstream from the antenna show a roughly constant electron temperature and a slight decrease of electron density up to ~30% He [see Fig. 7(a)]. For this gas mixture, the eedf is clamped by the Ar ionization potential and He ionization is rare. Although the total gas pressure monotonically decreases, at ~30% He fraction there is a sudden change in the slope of electron density and electron temperature curves. The electron temperature jumps from ~7 eV for pure argon up to ~14 eV for a helium fraction of 80%. At the same time, the electron density drops by more than three orders of magnitude from 1.14×10^{11} cm^{-3} to 6.5×10^{7} cm^{-3}. This behavior is quite different than for Ar–Xe case, where monotonic variations of the electron temperature and electron density were observed. The abrupt change in plasma parameters likely indicates a helicon (W) to inductive (H) transition and/or an even further inductive to capacitive (E) transition.

In agreement with the experimental measurements, the computed ion densities based on the measured electron density and electron temperature, relative species abundance, and the calculated ionization rate coefficients suggest that argon ions far outnumber helium ions in these mixed gas plasmas. Because the three orders of magnitude variation in absolute plasma density makes plots of the absolute densities difficult to discuss, we show the relative ionic composition in Fig. 7(b). For a 50/50 He/Ar mixture, Ar^+ makes up 93% of the total ion population.

The argon ions consistently dominate the plasma density, even for an 80/20 He/Ar mixing ratio. The much larger argon ion density is again explained by the large differences in the helium and argon ionization potentials (24.58 eV for He versus 15.76 eV for Ar) and the ionization cross-sections (peak value of 3.5×10^{-17} cm^2 for He versus 2.8×10^{-16} cm^2 for Ar).

V. DISCUSSION

Langmuir probe and optical emission spectroscopy investigations of mixed gas expanding helicon plasmas reveal the following features:.

(a) For an Ar–Xe plasma, the eedfs exhibit a transition from a Maxwellian type electron distribution in pure argon plasma to a Druyvesteyn type electron distribution for xenon fractions greater than a few percent. Another striking change of the eedf shape is the depletion of the high energy tail of the distribution with increasing xenon fraction. The maximum electron energies in the tail decrease by ~15 eV for pure xenon compared to pure argon. Both in the helicon source and in the expansion region, the increasing xenon fraction leads to an exponential decrease of the electron temperature. In HELIX the effective electron temperature decreases from 6.5 eV in pure argon to 3.8 eV in pure xenon. Similar variation is observed in LEIA, the electron temperature decreases from 7.2 to 4.7 eV. Electron densities calculated from the eedfs show a linear increase with increasing xenon fraction: in HELIX the density increases from 1.07×10^{11} to 1.25×10^{11} cm^{-3}, whereas in LEIA the density increases from 2×10^{9} to 5×10^{9} cm^{-3}. No high energetic electron population streaming through the EDL into HELIX (Ref. 49) was observed.
The optical emission spectroscopy investigation of the Ar I 811.75 nm and Xe I 823.39 nm emission line intensities enabled estimation of neutral gas relative densities and correlation with individual gas flow rates. The partial Ar^{+} density has an exponential decrease with the xenon fraction, whereas Xe^{+} density has a logarithmic increase with increasing Xe fraction. As a result of the large differences in ionization potentials and ionization cross-sections of Ar and Xe for xenon fraction higher than 10% the xenon ion density exceeds the argon ion density.

(b) As a result of the large differences in the ionization potentials and the ionization cross-section peak values of argon and helium, changing the gas composition in Ar–He plasma produces large variations in both electron temperature and plasma density. There is a twofold increase in the electron temperature with increasing helium fraction from ~7 eV for pure argon plasma up to ~14 eV for a helium fraction of 80%. Over the same helium fraction range, the electron density drops by more than three orders of magnitude from 1.14×10^{11} cm^{-3} down to 6.5×10^{7} cm^{-3}. Because the eedf is clamped by argon ionization potential, argon ions dominate the plasma density. Computed ion densities based on measured electron density and calculated ionization rate coefficients for each ion species suggest that ion population is dominated by Ar: at 50% He and 80% He the Ar^{+} population represents ~93% and 70% of the total ion population, respectively.

ACKNOWLEDGMENTS

The authors are thankful to Dr. Costel Biloiu now with Varian Semiconductor Equipment Associates for many enlightening discussions on LP and OES. This work was supported by NSF Award No. PHY-0611571.

[1] C. Charles, Plasma Sources Sci. Technol. **16**, R1 (2007).
[2] B. W. Longmier, J. P. Squire, M. D. Carter, L. D. Cassady, T. W. Glover, W. J. Chancery, C. S. Olsen, A. V. Ilin, G. E. McCaskill, and F. R. Chang Díaz, Proceedings of the 45th AIAA/ASME/SAE/ASEE Joint Propulsion Conference and Exhibit, Denver, 2009, Vol. 14, AIAA Paper No. 5359.
[3] C. Charles, J. Phys. D **42**, 163001 (2009).
[4] I. A. Biloiu, E. E. Scime, and C. Biloiu, Appl. Phys. Lett. **92**, 191502 (2008).
[5] K. Takahashi, C. Charles, R. Boswell, M. A. Lieberman, and R. Hatakeyama, J. Phys. D **43**, 162001 (2010).
[6] X. Sun, A. M. Keesee, C. Biloiu, E. E. Scime, A. Meige, C. Charles, and R. W. Boswell, Phys. Rev. Lett. **95**, 025004 (2005).
[7] M. D. West, C. Charles, and R. W. Boswell, J. Phys. D **42**, 245201 (2009).
[8] C. Charles, R. W. Boswell, R. Laine, and P. MacLellan, J. Phys. D **41**, 175213 (2008).
[9] S. Popescu, Y. Ohtsu, and H. Fujita, Phys. Rev. E **73**, 066405 (2006).
[10] N. Plihon, C. S. Corr, and P. Chabert, Appl. Phys. Lett. **86**, 091501 (2005).
[11] N. Plihon, C. S. Corr, P. Chabert, and J. L. Raimbault, J. Appl. Phys. **98**, 023306 (2005).
[12] N. Plihon, P. Chabert, and C. S. Corr, Phys. Plasmas **14**, 013506 (2007).
[13] F. F. Chen, IEEE Trans. Plasma Sci. **36**, 2095 (2008).
[14] K. Takahashi and T. Fujiwara, Appl. Phys. Lett. **94**, 061502 (2009).
[15] V. F. Virko, Yu. V. Virko, V. M. Slobodyan, and K. P. Shamrai, Plasma Sources Sci. Technol. **19**, 015004 (2010).
[16] K. Takahashi, Y. Shida, T. Fujiwara, and K. Oguni, IEEE Trans. Plasma Sci. **37**, 1532 (2009).
[17] K. P. Shamrai, V. F. Virko, Yu. V. Virko, and K. Toki, Bull. Am. Phys. Soc. **52**, 133 (2007).
[18] H. M. Mott-Smith and I. Langmuir, Phys. Rev. **28**, 727 (1926).
[19] I. D. Sudit and F. F. Chen, Plasma Sources Sci. Technol. **3**, 162 (1994).
[20] J. G. Laframboise and J. Rubinstein, Phys. Fluids **19**, 1900 (1976).
[21] I. H. Hutchinson, *Principles of Plasma Diagnostics* (Cambridge University Press, Cambridge, 1987), p. 70.
[22] I. A. Biloiu, "Laser induced fluorescence studies of ion acceleration in single and multiple species expanding plasmas," Ph.D. thesis, West Virginia University, 2009, http://ulysses.phys.wvu.edu/~plasma/Biloiu_Ioana_dissertation.pdf.
[23] I. D. Sudit and R. C. Woods, Rev. Sci. Instrum. **64**, 2440 (1993).
[24] M. J. Druyvesteyn, Z. Phys. **64**, 781 (1930).
[25] V. A. Godyak, Workshop on Radio-Frequency Discharges, All Hallows College, Dublin, Ireland, 2007.
[26] V. A. Godyak, R. B. Piejak, and B. M. Alexandrovich, Plasma Sources Sci. Technol. **1**, 36 (1992).
[27] T. E. Sheridan, M. J. Goeckner, and J. Goree, Jpn. J. Appl. Phys., Part 1 **34**, 4977 (1995).
[28] F. F. Chen, The XXX-th IEEE-ICOPS Meeting-Mini-Course on Plasma Diagnostics, Jeju, Korea, 2003.
[29] S. Knappmiller, S. Robertson, and Z. Sternovsky, Phys. Rev. E **73**, 066402 (2006).
[30] X. Sun, "A study of ion acceleration, asymmetric optical pumping and low frequency waves in two expanding helicon plasmas," Ph.D. thesis, West Virginia University, 2005, http://ulysses.phys.wvu.edu/~plasma/sunphd-2005.pdf.
[31] V. M. Donnelly, J. Phys. D **37**, R217 (2004).
[32] G. A. Hebner and P. A. Miller, J. Appl. Phys. **87**, 8304 (2000).
[33] C. Biloiu, X. Sun, E. Scime, and I. A. Biloiu, J. Appl. Phys. **102**, 053303 (2007).
[34] NIST atomic spectral lines database, http://www.nist.gov.
[35] C. Biloiu, X. Sun, Z. Harvey, and E. Scime, J. Appl. Phys. **101**, 073303 (2007).
[36] M. Schulze, A. Yanguas-Gil, A. von Keudell, and P. Awakowitz, J. Phys. D **41**, 065206 (2008).

[37]C. Scharwitz and T. Makabe, J. Appl. Phys. **106**, 113304 (2009).
[38]J. B. Boffard, C. C. Lin, and C. A. DeJoseph, J. Phys. D **37**, R143 (2004).
[39]J. B. Boffard, B. Ciaro, T. Weber, and C. C. Lin, At. Data Nucl. Data Tables **93**, 831 (2007).
[40]Y.-H. Chiu, B. L. Austin, S. Williams, R. A. Dressler, and G. F. Karabadzhak, J. Appl. Phys. **99**, 113304 (2006).
[41]J. T. Fons and C. C. Lin, Phys. Rev. A **58**, 4603 (1998).
[42]T. Czerwiec and D. B. Graves, J. Phys. D **37**, 2827 (2004).
[43]A. M. Keesee and E. E. Scime, Plasma Sources Sci. Technol. **16**, 742 (2007).
[44]K. H. Bai, H. Y. Chang, and H. S. Uhm, Appl. Phys. Lett. **79**, 1596 (2001).
[45]V. Godyak, IEEE Trans. Plasma Sci. **34**, 755 (2006).
[46]N. Y. Babaeva, J. K. Lee, and J. W. Shon, J. Phys. D **38**, 287 (2005).
[47]F. F. Chen, G. D. Evans, and D. Arnush, Phys. Plasmas **9**, 1449 (2002).
[48]G. J. H. Brussaard, M. van der Steen, M. Carrere, M. C. M. van de Sanden, and D. C. Schram, Phys. Rev. E **54**, 1906 (1996).
[49]K. Takahashi, C. Charles, R. Boswell, W. Cox, and R. Hatakeyama, Appl. Phys. Lett. **94**, 191503 (2009).